Displacement correction for punching at a dynamically loaded bar end

Kamal Safa, Gérard Gary

Displacement correction for punching at a dynamically loaded bar end

K. Safa, G. Gary*

Laboratoire de Mécanique des Solides, Ecole Polytechnique, 91128 Palaiseau, France

The object of this work is to provide a 3-D displacement correction for local punching due to axial load at the end of a bar. For this purpose, an analytical calculation of the indentation at the end of an elastic isotropic bar subjected to a dynamic loading is carried out. It provides a first-order correction of the displacement obtained through the 1-D wave analysis commonly used in SHPB processing. This correction improves the results obtained for the dynamic behavior of the specimen, in particular at early instants of loading where its response is often purely elastic. Tabulated values are provided for easy use in SHPB testing.

1. Introduction

We are interested in the evaluation of the local displacement induced at the end of a bar by a central axial load, a phenomenon referred to as punching. The elementary 1-D theory of wave propagation in bars, and also some more advanced theories that consider wave dispersion due to lateral inertia effects [1–3], do not tackle this problem. Rather they investigate wave propagation at large distances from the bar end [4]. The determination of the local displacement at a bar end is of practical importance for the use of the SHPB device, as suggested by some authors [5].

The SHPB device, also called Kolsky apparatus, is widely used to measure the stress–strain behavior of materials at high rates of loading. This behavior is derived from the forces and velocities at the specimen faces. These quantities are obtained from the axial strains recorded by use of strain gauges glued to the sides of the input and output bars. The 1-D force deduced from this measured strain is assumed to be equal to the resulting applied force at the end of the bar, as validated in [6,7]. These forces and speeds allow for the use of inverse methods to investigate the specimen behavior [8]. A particular use of such methods is to compute the initially elastic response of the specimen as it was proposed in [9] for an optimized determination of the relative position of the origin of the three waves involved. This technique has been intensively used in our laboratory [10], where we have observed that the calculated value of the Young's modulus of the specimen is always smaller, in particular with small-diameter specimens, than the expected or known value. We have suspected that this systematic error was due to an imperfect measurement of the average strain of the specimen. The bar face in contact with the specimen does not remain plane as it is non-uniformly loaded, i.e. subjected to a local elastic punching. The corresponding displacement field is restricted to the impact zone and is not recorded by the strain gauges located far from the bar end. This is in agreement with a recommendation for SHPB found in the book of Buchar, Bilek and Dusek [11], that the specimen diameter must be large enough compared with that of the bars (less than 10% difference).

We propose to determine more accurately the displacement of the bar face by use of a local 3-D approach divided into two parts. The first part is based on transient wave analysis, valid at the early instants of loading. Oliver [12], followed by Safford [13], addressing the force measurement at these early instants, mentioned some limitations of the Pochhamer and Chree model to describe a punctual loading. Field et al. [14] mentioned the local displacement due to the indentation of a half space. In the second part of the solution of our problem that applies at later times, a quasi-static analysis is used. This problem has been studied by Knowles and Horgan [15] who only addressed the force measurement. The quasi-static solution that we obtain is the same as the dynamic, except for highest frequencies seen as radial oscillations of the section of the bar. The temporal juxtaposition of both solutions gives an estimation of the punching displacement.

* Corresponding author.
E-mail addresses: Safa@lms.polytechnique.fr (K. Safa), Gary@lms.polytechnique.fr (G. Gary).

Nomenclature

$p(t)$	Average local axial displacement under the specimen (called punching displacement in the paper)
$u(t)$	Axial displacement at the specimen–bar interface obtained by classical SHPB processing
$F(t)$	Axial force applied on the specimen measured by the SHPB device
$\sigma(t)$	Axial stress in the specimen, corresponding to $F(t)$
$J_n(x)$	Bessel function of the first kind
	$k_1 = \sqrt{1 - c_R^2/c_1^2}$, $q_1 = \sqrt{1 - c_R^2/c_2^2}$.
c_1, c_2	Dilatational and shear waves velocities in a medium
λ, μ	Lame's parameters for the constitutive material of the input or output bar
c_0	Longitudinal waves velocity in a thin rod
ν	Poisson ratio
K_p	Punching correction coefficient. $1/K_p$ is homogeneous to a spring stiffness
r	Radial cylindrical coordinate
R	Radius of the SHPB input or output bar
a	Radius of the specimen
α	Rate of the axial stress in the specimen at the beginning of the loading, assumed as constant $\sigma(t) = \alpha t$
ρ	Ratio of the radial coordinate of a point to that of the input or output bar $\rho = r/R$
ρ_a	Ratio of the specimen radius to that of the input or output bar $\rho_a = a/R$
c_R	Rayleigh (surface) waves velocity
$K(x)$, $E(x)$	Respectively the complete elliptic integrals of the first and second kind, respectively
t_1	Time after which the punching correction $p(t)$ becomes valid
t	Time variable
$d(t)$	Total average displacement under the specimen $d(t) = u(t) + p(t)$

Numerical and experimental studies were also carried out. They provide estimations of the consequence of the proposed displacement correction to the dynamic response of a specimen. A closed-form expression for this correction is provided that has practical advantages for implementation. The correction is especially significant at the beginning of the loading where it permits estimation of the elastic modulus of the tested material. Tabulated values are provided for easy use in SHPB testing.

2. Statement of the problem

A typical SHPB device for compression testing is shown in Fig. 1. Three waves are involved in the experiment: an incident compressive wave generated by the impact of the striker, a reflected tensile wave due to the lower impedance of the specimen, and a transmitted compressive wave. The incident and reflected waves $\varepsilon_i(x, t)$ and $\varepsilon_r(x, t)$ are recorded at gauge A of the input bar and the transmitted wave $\varepsilon_t(x, t)$ at gauge B of the output bar.

By use of wave theory, usually taking account of dispersion, the strains measured at A and B are obtained at the bar–specimen interfaces. Forces, velocities and displacements at each bar face are obtained subsequently.

In Fig. 2, the sample is shown together with the output bar, with a deformed configuration of the bar end under a uniformly distributed force $F(t)$. The SHPB displacement is $u(t)$. The additional displacement $p(t)$ resulting from the local elastic 3-D axisymmetric deformation of the bar is referred to as elastic punching. It appears when the diameter of the specimen is smaller than that of the bar. The determination of the elastic punching makes it possible to correct the SHPB measured 1-D displacement and to obtain the displacement at the specimen–bar interface as $d(t) = u(t) + p(t)$.

We make the following assumptions which are usually accepted in SHPB practice:

- The friction between the sample and the bar faces is negligible.
- The uniaxial stresses within the specimen are uniformly distributed through the cross section.

Based on these two assumptions, the problem becomes that of a semi-infinite elastic bar with traction-free lateral faces, axisymmetrically loaded at its end by a uniform distribution of time-dependent normal stress. The resulting force $F(t)$ and the corresponding uniform axial stress in the specimen $\sigma(t)$ are assumed to be known. The 3-D dynamic problem can be solved to a good approximation through superposition of the 1-D dynamic and a 3-D quasi-static loading solutions, as shown in Fig. 3.

- The first loading case is obtained by applying a uniform stress to the whole section of the bar such that the resulting force equals $F(t)$. This case can be approximated as a 1-D dynamical loading case, provided that the highest frequencies f in the

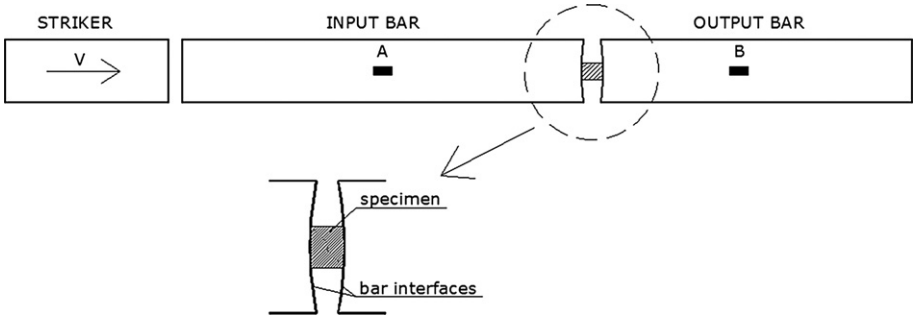

Fig. 1. Split Hopkinson pressure bar (SHPB) setup.

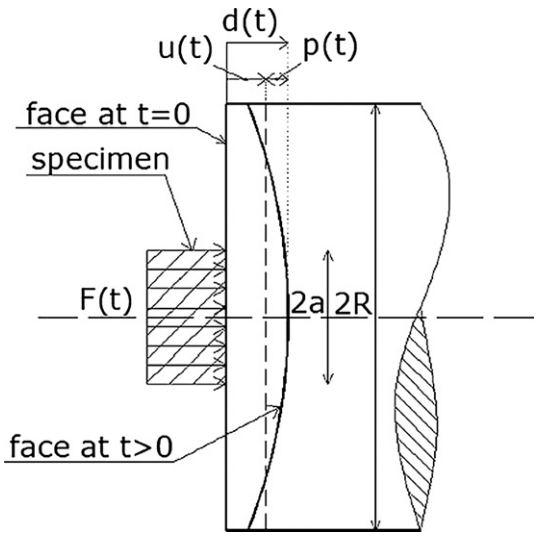

Fig. 2. Shape of the bar end at the bar–specimen interface.

spectrum of the force are negligible compared with $c_0/2R$ [16]. The displacement $u(t)$ derived from this 1-D case is that of the classical SHPB processing.

– The second loading case is obtained by the application of a quasi-static self-equilibrated load as shown in Fig. 3. This configuration leads to vanishing displacements far from the loading zone and produces a local displacement $p(t)$, thus providing a quasi-static approximation of the dynamic punching. At some time after impact, the waves propagating radially at the bar end tend to a quasi-static state. This approximation is valid if the load duration is large enough compared with the time needed by the surface waves to make several transits along the radius of the bar.

The quasi-static nature of this solution in the framework of small displacements means that it can be expressed in terms of a linear relation $p(t) = K_p F(t)$ between the total force $F(t)$and the average punching $p(t)$ linked by a constant K_p that depends on the specimen and bar diameters and the elastic constants of the bar.

At the very early instants of the loading, when the reflected waves at the lateral sides of the cylinder have not yet superimposed, the above analysis (referred to as problem B in the following) is not valid. The problem is therefore that of a half space suddenly loaded by a time-varying force. This will be referred to as problem A in the following.

3. Mathematical formulation

Cylindrical coordinates (r, θ, z) are used. In the axisymmetric case considered, the non-zero components of displacement are u_r and u_z and those of stress are σ_r, σ_θ, σ_z and σ_{rz}. The normal stress applied to the specimen is $\sigma(t) = F(t)/\pi a^2$, where a is the radius of the specimen. Fig. 4 shows the typical evolution of the axial stress $\sigma(t)$ in the specimen (in the present example: brass specimen Ø5-H5 mm; SHPB diameters 20 mm; average strain rate 80 s^{-1}).The boundary conditions are, for $z = 0$,

$$\sigma_z = \sigma(t), \quad 0 \le r < a \tag{1}$$

$$\sigma_z = 0, \quad a < r \le R \tag{2}$$

$$\sigma_{rz} = 0, \quad 0 \le r \le R \tag{3}$$

and for $r = R$;

$$\sigma_r = \sigma_{rz} = 0, \quad 0 \le z \tag{4}$$

The initial conditions are

$$\sigma_r = \sigma_z = \sigma_\theta = \sigma_{rz} = 0, \tag{5}$$

$$u_r = u_z = \dot{u}_r = \dot{u}_z = 0. \tag{6}$$

The equations of motion are

$$(\lambda+2\mu)\left(\frac{\partial^2 u_r}{\partial r^2}+\frac{1}{r}\frac{\partial u_r}{\partial r}-\frac{u_r}{r^2}\right)+\mu\frac{\partial^2 u_r}{\partial z^2}+(\lambda+\mu)\frac{\partial^2 u_z}{\partial r\partial z}=\rho\frac{\partial^2 u_r}{\partial t^2} \tag{7}$$

$$(\lambda+\mu)\left(\frac{\partial^2 u_r}{\partial r\partial z}+\frac{1}{r}\frac{\partial u_r}{\partial z}\right)+\mu\left(\frac{\partial^2 u_z}{\partial r^2}+\frac{1}{r}\frac{\partial u_z}{\partial r}\right)+(\lambda+2\mu)\frac{\partial^2 u_z}{\partial z^2} = \rho\frac{\partial^2 u_z}{\partial t^2}, \tag{8}$$

where λ, μ are Lamé's parameters for the bar material. In terms of these parameters, the dilatational and shear waves velocities are $c_1 = \sqrt{(\lambda+2\mu)/(\rho)}$ and $c_2 = \sqrt{(\mu)/(\rho)}$, respectively. In the quasi-static case, the acceleration terms vanish.

As mentioned before, the problem is divided in two parts. At early instants, (Problem A), the waves produced by the loading are the same as they would be in a semi-infinite solid. This state lasts as

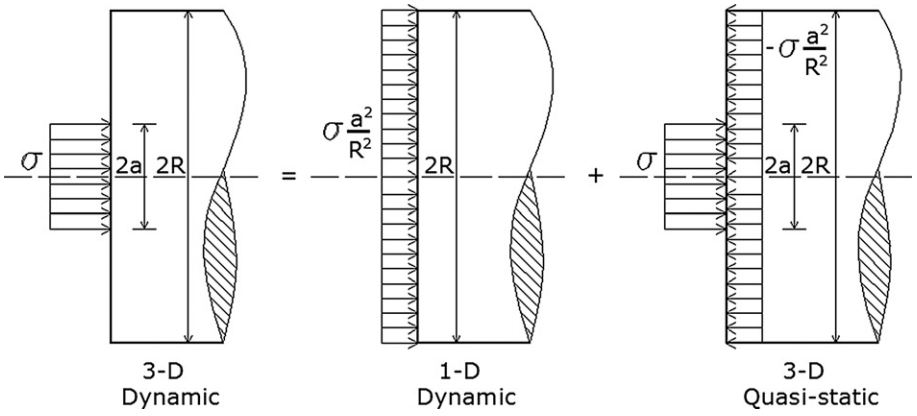

Fig. 3. Determination of the local displacement $p(t)$ by superposition of states of stresses.

long as the reflected waves at the free cylindrical surface of the bar are not superimposed. The solution of Problem A is therefore valid for a very short time t_1 (if compared with the SHPB test duration). After a time much larger than t_1, the waves propagating radially at the bar end tend to a quasi-static state while the axial waves produced early on in the loading are now far from the end of the bar (Problem B). It will be shown that the solution of this problem provides a sufficient correction for punching in SHPB applications.

4. Solution of problem A

This first part of the solution concerns the determination of the displacement during the first stage of the loading. We assume that, at this stage, the loading is approximated by stresses varying linearly with time (Fig. 4). In terms of the Heaviside step function, the boundary condition at the end of the bar can be written

$$\sigma_z = \alpha t H(a-r)H(t). \tag{9}$$

The procedure used here is to apply the Laplace and Hankel transforms to the equations of motion. To ensure the validity of the solution, we have to assume that the waves reflected at the sides of the cylinder have no influence on the displacement that we are looking for, as would be the case for a half-space. This assumption is true until a time t_1 (to be determined later). The method that follows is similar to the one used in [17,18] for a half-space medium suddenly loaded.The Laplace transform of a function f is defined as $\overline{f}(s) = \int_0^\infty f(t)e^{-st}\mathrm{d}t$. By applying the Laplace transform to Eqs. (7) and (8) we obtain:

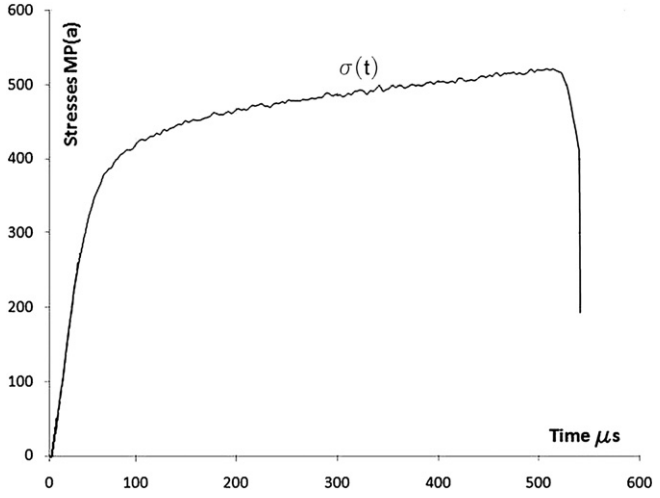

Fig. 4. Experimental axial stress curve $\sigma(t)$.

$$c_1^2\left(\frac{\partial^2\overline{u}_r}{\partial r}+\frac{1}{r}\frac{\partial\overline{u}_r}{\partial r}-\frac{\overline{u}_r}{r^2}\right)+c_2^2\frac{\partial^2\overline{u}_r}{\partial z^2}+\left(c_1^2-c_2^2\right)\frac{\partial^2\overline{u}_z}{\partial r\partial z}=s^2\overline{u}_r \tag{10}$$

$$\left(c_1^2-c_2^2\right)\left(\frac{\partial^2\overline{u}_r}{\partial r\partial z}+\frac{1}{r}\frac{\partial\overline{u}_r}{\partial z}\right)+c_2^2\left(\frac{\partial^2\overline{u}_z}{\partial r^2}+\frac{1}{r}\frac{\partial\overline{u}_z}{\partial r}\right)+c_1^2\frac{\partial^2\overline{u}_z}{\partial z^2}=s^2\overline{u}_z. \tag{11}$$

The Hankel transform of a function f is defined by $\widetilde{f}(\xi) = \int_0^\infty J_n(\xi r)f(r)r\mathrm{d}r$, where $J_n(\xi r)$ are Bessel functions of the first kind. By multiplying Eqs. (10) and (11) by $J_1(\xi r)r$, $J_0(\xi r)r$, respectively, and integrating with respect to r from 0 to ∞, we obtain

$$c_2^2\frac{\partial^2}{\partial z^2}-c_1^2\xi^2-s^2\Big)\widetilde{\overline{u}}_r-\left(c_1^2-c_2^2\right)\xi\frac{\partial\widetilde{\overline{u}}_z}{\partial z}=0 \tag{12}$$

$$c_1^2\frac{\partial^2}{\partial z^2}-c_2^2\xi^2-s^2\Big)\widetilde{\overline{u}}_z-\left(c_1^2-c_2^2\right)\xi\frac{\partial\widetilde{\overline{u}}_r}{\partial z}=0. \tag{13}$$

These equations have the general solution

$$\widetilde{\overline{u}}_r = Ae^{-kz}+Be^{-qz} \tag{14}$$

$$\widetilde{\overline{u}}_z = Ce^{-kz}+De^{-qz}, \tag{15}$$

where $k=\sqrt{\xi^2+(s^2)/(c_1^2)}$; $q=\sqrt{\xi^2+(s^2)/(c_2^2)}$. Putting Eqs. (14) and (15) into Eqs. (12) and (13), we obtain $C=(k/\xi)A$; $D=(\xi/q)B$ which gives

$$\widetilde{\overline{u}}_r = Ae^{-kz}+Be^{-qz} \tag{16}$$

$$\widetilde{\overline{u}}_z = \frac{k}{\xi}Ae^{-kz}+\frac{\xi}{q}Be^{-qz}. \tag{17}$$

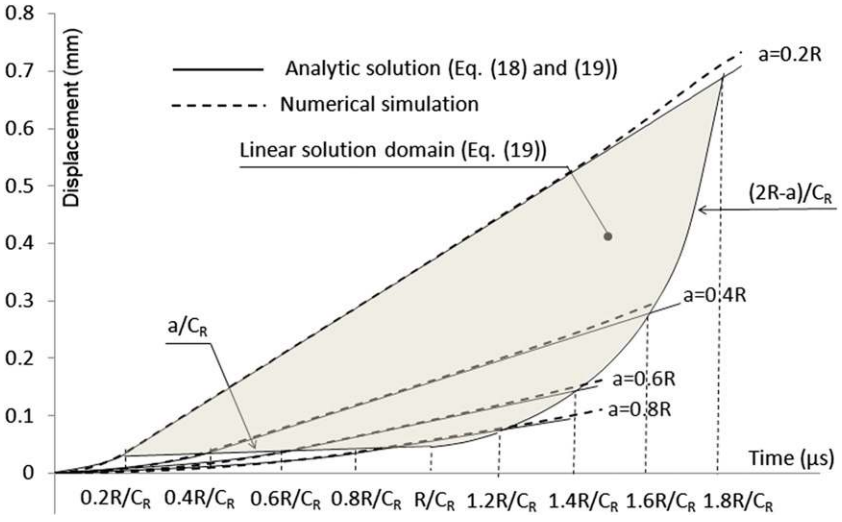

Fig. 5. Axial displacement at the origin (0, 0) for a cylinder of radius R subjected to uniform distributions of pressure of different radii a_i applied linearly with time.

The parameters A and B are obtained from the boundary conditions for $\widetilde{\overline{\sigma}}_z$ and $\widetilde{\overline{\sigma}}_{rz}$ at $z=0$. Their derivation and subsequent results are given in Appendix 1 and summarized here. When $\widetilde{\overline{u}}_r$ and $\widetilde{\overline{u}}_z$ are obtained, applying the inverse Laplace transform leads to a complex integral. Its solution relies on the use on Cauchy's residue theorem. Applying the inverse Hankel transform to this solution, one finally obtains the axial surface displacement under a specimen of radius a at radius $r \le a$ and time t. (Eqs. (71) and (72)). It becomes

$$u_z = -\frac{a\alpha}{\mu}\left\{\frac{2}{\pi}(1-\nu)E\left(\frac{r}{a}\right)t + \frac{k_1 c_R \int_0^{\pi} \frac{a - r\cos\phi}{W^2}\left(c_R t\sqrt{W^2 - c_R^2 t^2} + W^2 \arcsin\frac{c_R t}{W}\right)\mathrm{d}\phi}{8c_2^2\left[\frac{c_R^2}{c_2^2}\left(2 - \frac{c_R^2}{c_2^2}\right) - \frac{q_1 c_R^2}{k_1 c_1^2} - \frac{k_1 c_R^2}{q_1 c_2^2}\right]}\right\} \tag{18}$$

for $c_R t < (a+r)$, and

$$u_z = -\frac{a\alpha}{\mu}\left\{\frac{2}{\pi}(1-\nu)E\left(\frac{r}{a}\right)t + \frac{\pi^2 k_1 c_R a}{16c_2^2\left[\frac{c_R^2}{c_2^2}\left(2 - \frac{c_R^2}{c_2^2}\right) - \frac{q_1 c_R^2}{k_1 c_1^2} - \frac{k_1 c_R^2}{q_1 c_2^2}\right]}\right\} \tag{19}$$

for $c_R t \ge (a+r)$.

The conditions leading to Eq. (18) or to Eq. (19) define a time $t_r = (a+r)/c_R$ for which the Rayleigh waves propagating from every part of the loaded area have reached the point at radius r, as $(a+r)$ is the distance of the most distant point.

We recognize the first term of Eq. (18) as the quasi-static displacement of a half-space subjected to a disk $r<a$ of uniform pressure αt [19] (chapter 13 §124). The second term of Eq. (18) which is a function of time for $t<t_r$ reduces to a constant for $t \ge t_r$. Then, Eq. (19) shows that the displacement at any point of the loaded area is a linear function of time for $t \ge t_r$. The greatest possible value of t_r is obtained when $r=a$. Consequently, the solution for Problem A shows the existence, for $t > 2a/c_R$, of a displacement that increases linearly with time in every part $0<r<a$ of the loaded area. In order to illustrate the above result and to obtain the time t_1 after which this solution diverges from that for a cylinder, the displacement at the origin ($r=0$) is compared in Fig. 5 with that obtained from numerical simulations (see Appendix 3) for a cylinder of radius R subjected to the same force uniformly distributed over disks of different radii $0<a<R$. In this particular case ($r=0$) the response is linear with time for $t > a/c_R$. It is expected that this holds true until the first return of Rayleigh waves from the lateral surface of the cylinder, that is, for $a/c_R < t < (2R-a)/c_R$. The linear parts of the solutions, given by Eq. (19), are plotted for each case of loading. We notice that as a becomes closer to R, this linear solution lasts a shorter and shorter time till it vanishes at $a=R$. The values of a/c_R give the time where starts the linear time–displacement relation (Eq. (19)), while those of $(2R-a)/c_R$ correspond to its upper limit after which the half-space solution is no longer applicable. The intensity of the force being unchanged, the corresponding domain is limited by a horizontal line (t varying with a/c_R) and a hyperbola (t varying with $(2R-a)/c_R$). This domain (hatched in Fig. 5) represents the interval of time corresponding to each loaded diameter where the displacement at the point $r=0$ is obtained by Eq. (19).

The average axial displacement u_0 under the sample at a given time t can be obtained by integrating Eq. (19) along $r \le a$. It gives

$$u_0(t) = \frac{1}{\pi a^2}\int_0^a 2\pi u_z r\mathrm{d}r = \frac{a\alpha}{\mu}\left\{\frac{8}{3\pi}(1-\nu)t + \frac{\pi^2 k_1 a}{32c_R\left[4q_1 k_1 - \frac{q_1}{k_1}\frac{1-2\nu}{2(1-\nu)} - \frac{k_1}{q_1}\right]}\right\}, \tag{20}$$

where $k_1 = \sqrt{1-(c_R^2)/(c_1^2)}$; $\quad q_1 = \sqrt{1-(c_R^2)/(c_2^2)}$.

This integration is valid provided that Eq. (19) applies for any value of r such as $0<r\le a$. Consequently it applies for $2a/c_R < t < t_1$. $t_1 = 2(R-a)/c_R$ is the time needed by Rayleigh waves to travel forth and back between the edge of the specimen and that of the bar.

We now have to calculate the displacement at the bar end for $t > t_1$.

5. Solution of problem B

As explained in the statement of the problem, to determine the correction $p(t)$ at large times we consider the quasi-static self-equilibrated end-loading problem of a semi-infinite cylinder. The solution of this problem will provide the correction $p(t)$ to be added to the measured displacement $u(t)$ at any time $t > t_1$. In this section the force $F(t)$ can be of any form.

The problem of self-equilibrated axisymmetric loadings acting on the ends of a cylinder with stress-free lateral sides has received wide attention in the frame of the theory of elasticity. The solutions hold true for any value of the load. A solution in the form of eigenfunction expansions has been proposed by Lurie [20] (Section 5.7.9). The method consists in finding a set of tractions (of the desired form) at the end surface that approximates the exact boundary conditions (the least squares method of error control is used). The unknown quantities that multiply the eigenvalues in the eigenfunction expansions are called participation factors, and cannot be directly obtained because these expansions are not orthogonal.

Later, Little and Childs [21] developed a set of orthogonal vectors that allow the determination of the participation factors in a direct way but only for the case of mixed boundary conditions (traction and displacement prescribed at the plane face). When only tractions are prescribed, the participation factors need to be obtained by truncation of an infinite set of equations. Horvay and Mirabal

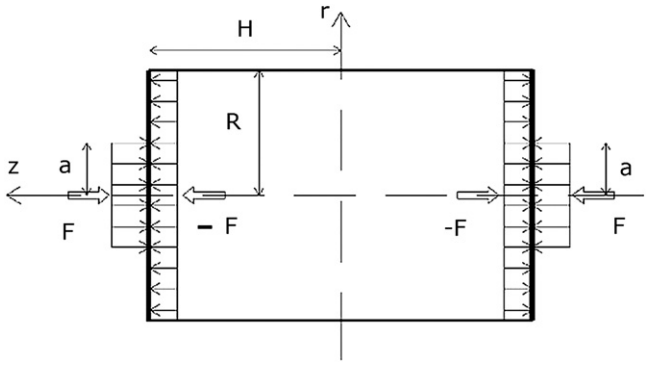

Fig. 6. Long cylinder ($H > 2R$) subjected to self-equilibrated tractions with resultant F.

[22] have proposed another approach for the problem based on the use of a variational approximate solution that did not present practical advantages and was lacking completeness [23]. These methods have been used to solve particular end-loading problems, mainly the thermal one. The prescribed tractions on the end face when using the methods mentioned are continuous and slowly varying from the center of the cylinder to its boundary. In the case of discontinuous and irregular loading functions, as in our case, the convenient way to approach the cylinder problem is to expand the tractions on the end face in Fourier–Bessel series. Benthem and Minderhood [24] solved the problem of a cylinder compressed between two rough rigid stamps by using the orthogonal functions of Little and Childs [21] and by developing the stresses at the boundary in Fourier–Bessel series. Recently, Wei et al. [25] developed a displacement potential for solving the axisymmetric problem of a finite cylinder subjected to rigid axisymmetric indenters. Even though this solution applies for finite cylinders, the exponential stress decay near the boundary leads to the same field of stresses as the one in semi-infinite cylinders subjected to the same tractions [20] (Section 5.7.9). This happens, in particular, when the end face of the cylinder is subjected to self-equilibrated stresses, and when the length-to-diameter ratio is large.

We consider a cylinder of diameter $2R$ and height $2H(H>2R)$ subjected on its plane surfaces to self-equilibrated stresses, each corresponding to a total normal force F, considered at any time $(t>t_1)$. The origin of the cylindrical coordinates $(r,\ \theta,\ z)$ is at the center of the cylinder (Fig. 6).

The axial component of the displacement (denoted here as p_z) is expressed in terms of the displacement potential Φ as [26]:

$$p_z = -\left[2(1-\nu)\ \frac{\partial^2}{\partial r^2}+\frac{1}{r}\frac{\partial}{\partial r}\right)\Phi+(1-2\nu)\frac{\partial^2\Phi}{\partial z^2}\Bigg]. \tag{21}$$

The expressions for the normal and shear stresses in terms of the potential Φ are [26]

$$\sigma_z = -2\mu\left[(2-\nu)\frac{\partial}{\partial z}\nabla^2-\frac{\partial^3}{\partial z^3}\right]\Phi \tag{22}$$

$$\sigma_{rz} = -2\mu\left[-(1-\nu)\ \frac{\partial^3}{\partial r^3}+\frac{\partial}{\partial r}\left(\frac{\partial}{r\partial r}\right)\right)+\nu\frac{\partial^3}{\partial r\partial z^2}\Bigg]\Phi \tag{23}$$

$$\sigma_r = -2\nu\mu\nabla^2\frac{\partial\Phi}{\partial z}+2\mu\frac{\partial^3\Phi}{\partial z\partial r^2}, \tag{24}$$

where ∇^2 is the Laplace operator. The expression for the potential Φ is [25]:

$$\begin{aligned}\Phi = -\frac{R^3}{2\mu}\Bigg\{&A_0\frac{k^3\eta^3}{6}+C_0\frac{k\eta\rho^2}{2}+\sum_{n=1}^{\infty}\frac{\sin(n\pi\eta)}{\beta_n^3}[A_nI_0(\beta_n\rho)\\&+B_n\beta_n\rho I_1(\beta_n\rho)]+\sum_{s=1}^{\infty}\frac{J_0(\lambda_s\rho)}{\lambda_s^3}[C_s\sinh(\gamma_s\eta)\\&+D_s\gamma_s\eta\cosh(\gamma_s\eta)]\Bigg\},\end{aligned} \tag{25}$$

where $\rho=r/R,\quad \eta=z/H,\quad k=H/R,\quad \lambda_s$ is the s_{th} root of $J_1(x)=0,\quad \gamma_s=\lambda_s k,\quad \beta_n=n\pi/k$, and $A_0, C_0, A_n, B_n, C_s, D_s$ are the unknown coefficients to be determined by use of the boundary conditions. Substituting Eq. (25) into Eqs. (23) and (24), and applying the boundary conditions $\sigma_{rz}=\sigma_r=0$ at $\rho=1$ lead to the relations [25]:

$$A_0\nu+(2\nu-1)C_0 = 0 \tag{26}$$

$$E_n+\sum_{s=1}^{\infty}F_sQ_{sn} = 0 \tag{27}$$

between the unknown coefficients, where

$$Q_{sn} = \frac{4(-1)^n\gamma_s(n\pi)^2J_0(\lambda_s)\sinh^2\gamma_s}{\Omega_s\left(\gamma_s^2+(n\pi)^2\right)^2};\quad \Omega_s = \sinh\gamma_s\cosh\gamma_s+\gamma_s.$$

The coefficients E_n and F_s are related to the original unknowns A_n, B_n, C_s, D_s by the relations:

$$\begin{aligned}&\frac{A_n}{2(1-\nu)I_1(\beta_n)+\beta_nI_0(\beta_n)}\\&\quad=\frac{B_n}{-I_1(\beta_n)}=\frac{E_n}{\left[\left[2(1-\nu)+\beta_n^2\right]I_1^2(\beta_n)-\beta_n^2I_0^2(\beta_n)/\beta_n\right]}\end{aligned} \tag{28}$$

$$\frac{C_s}{2\nu\sinh\gamma_s+\gamma_s\cosh\gamma_s}=\frac{D_s}{-\sinh\gamma_s}=\frac{-F_s}{\Omega_s}. \tag{29}$$

To apply the boundary conditions on the flat surfaces of the cylinder $(\eta=\pm1)$, the tractions need to be expanded into Fourier–Bessel series. The boundary conditions at $\eta=\pm1$ are

$$\sigma_z = \begin{cases}-\dfrac{F}{\pi R^2\rho_a^2}+\dfrac{F}{\pi R^2} & \text{for}\quad \rho\le\rho_a\\ \frac{F}{\pi R^2} & \text{for}\quad \rho\le\rho_a\end{cases} \tag{30}$$

where $\rho_a = a/R$ .The Fourier–Bessel expansion of Eq. (30) is

$$\sigma_z = \frac{2F}{\pi\rho_aR^2}\sum_{s=1}^{\infty}\frac{J_1(\lambda_s\rho_a)}{\lambda_sJ_0^2(\lambda_s)}J_0(\lambda_s\rho). \tag{31}$$

Substituting Eq. (25) into Eq. (22) and identifying with Eq. (31) at $\eta=\pm1$, we obtain the relations

$$A_0(1-\nu)+2(2-\nu)C_0 = 0 \tag{32}$$

$$F_s+\sum_{n=1}^{\infty}E_nR_{sn} = \frac{2F}{\pi\rho_aR^2}\frac{J_1(\lambda_s\rho_a)}{\lambda_sJ_0^2(\lambda_s)} \tag{33}$$

between the unknown variables, where

$$R_{sn} = \frac{4(-1)^{(n+1)}\lambda_s^2\beta_n^2I_1^2(\beta_n)}{\left[\left[2(1-\nu)+\beta_n^2\right]I_1^2(\beta_n)-\beta_n^2I_0^2(\beta_n)\right]\left[\lambda_s^2+\beta_n^2\right]^2J_0(\lambda_s)}. \tag{34}$$

Equations (26), (27), (32) and (33) constitute a set of simultaneous equations from which coefficients A_0, C_0, F_s and E_n can be obtained by taking enough terms of the series in the calculation. A_0 and C_0 are equal to zero as implied by Eqs. (26) and (32) and represent a homogeneous state of stress. With the aid of these coefficients and Eq. (21), the displacements inside the cylinder can be calculated.

In order to obtain the displacements at the flat end of the cylinder, we substitute Eq. (25) into Eq. (21) and set $\eta=1$, which gives

$$p_z = \frac{1-\nu}{\mu} R \sum_{s=1}^{\infty} F_s \frac{J_0(\lambda_s \rho)\sinh^2 \gamma_s}{\lambda_s \Omega_s}. \quad (35)$$

6. A closed-form approximate expression for punching

Although Eq. (35) provides an analytical solution for the problem, some numerical calculations are needed to obtain a quantitative result. Moreover, it does not help for an estimation of the influence of the mechanical parameters of the problem. Therefore, we shall now search for an approximate closed-form expression for the average displacement under the specimen that will be more convenient for SHPB practice.

The displacement Eq. (35) depends on the material properties ν, ($\mu = G$), and the normalized variables ρ, ρ_a and η ($\rho = r/R$; $\rho_a = a/R$; $\eta = z/H$). The height of the cylinder is sufficient to ensure that at $\eta = 0$ (in the middle) the stresses and displacements tend to zero. This is verified for $(H/R) \geq 3$. When the boundary conditions have no influence on the stress and displacement fields at the center of the cylinder, it can be considered as "long" compared to the "short" cylinder ($\eta \leq 1$) in which the mechanical fields are nowhere homogenous.

The correction of the 1-D SHPB displacement u is especially significant when the radius of the specimen a is small. Moreover, it is expected from the above theoretical results, that the correction becomes very small when the specimen diameter is large. Consequently, the subsequent analysis is carried out for $0.1 \leq \rho_a \leq 0.5$. We are looking for the displacement under the specimen for: $0 \leq \rho \leq \rho_a$. The Poisson's ratio of the bar can take any value in the interval $0.1 \leq \nu \leq 0.4$. The Poisson's ratio occurs in Eq. (35) and inside the expression for R_{sn} in Eq. (34). We can evaluate its contribution in by writing Eq. (35) in the form: $p_z = (1-\nu)/(\mu)$, where the factor A is calculated for different values of ν. We find that A is almost independent of ν (less than 2% variation). Therefore the term $(1-\nu)/(\mu)$ sufficiently takes into account the material properties of the bar as far as p_z is concerned.

Eq. (33) shows that the variables F_s and E_n are proportional to $(2F)/(\pi\rho_a R^2)$ since this factor multiplies the second member of the simultaneous set of equations. As the displacement Eq. (35) is generated by a linear summation of F_s, it can be factorized by $(2F)/(\pi\rho_a R^2)$. By setting $G_s = (\pi\rho_a R^2/2F)F_s$ we can write Eq. (35) as

$$p_z = \frac{2(1-\nu F)}{\pi\mu R\rho_a} \sum_{s=1}^{\infty} G_s \frac{J_0(\lambda_s\rho)\sinh^2\gamma_s}{\lambda_s\Omega_s} = \frac{2(1-\nu)}{\pi\mu R\rho_a} M(\rho,\rho_a). \quad (36)$$

To identify the behavior of the series in Eq. (36) we consider the function $M(\rho,\rho_a) = \sum_{s=1}^{\infty} G_s(J_0(\lambda_s\rho)\sinh^2\gamma_s/\lambda_s\Omega_s)$ which we have plotted versus ρ_a for several values of ρ ($\rho = 0$, $\rho = 0.15$, $\rho = 0.30$, $\rho = \rho_a$) (Fig. 7).

Fig. 7 shows that $M(0, \rho_a)$ and $M(\rho_a, \rho_a)$ have characteristic forms and appear to be almost linear functions of ρ_a, i.e.,

$$M(0,\rho_a) = \frac{1}{2} - \frac{\rho_a}{2} \quad (37)$$

$$M(\rho_a,\rho_a) = \frac{1}{\pi} - g(\rho_a)\rho_a, \quad (38)$$

where $g(\rho_a)$ is the slope of $M(\rho_a, \rho_a)$, undetermined yet.

Substituting Eq. (37) into Eq. (36), we obtain the displacement at $r = 0$ for any value of $0 \leq \rho_a \leq 0.5$

$$p_z = \frac{1}{\pi}\frac{1-\nu}{\mu}\frac{1-\rho_a}{R\rho_a}F. \quad (39)$$

In order to obtain the displacement at any point under the specimen, we adopt the following procedure that starts by identifying $g(\rho_a)$. For this, we plot in Fig. 8 the function $g(\rho_a) = -(1/\rho_a)[M(\rho_a,\rho_a) - (1/\pi)]$.

Fig. 8 shows that $g(\rho_a)$ can be approximated by $(E(\rho_a))/(\pi)$ with an error less than 1%, where $g(\rho_a)$ is the complete elliptic integral of the second kind with argument ρ_a. The choice of the elliptic integral is also justified since $E(0)/\pi = 1/2$ constitutes the second term of Eq. (37). Now we suppose that $M(\rho, \rho_a)$ can be written as

$$M(\rho,\rho_a) = \frac{1}{\pi}(f(\rho,\rho_a) - E(\rho)\rho_a), \quad (40)$$

where $f(\rho, \rho_a)$ is a function for which two particular values are known: $f(0,\rho_a) = \pi/2$ and $f(\rho_a, \rho_a) = 1$ as deduced from Eq. (37).

In the same manner as for $g(\rho)$, we determine $f(\rho, \rho_a)$ by plotting the function $f(\rho, \rho_a) = \pi M(\rho, \rho_a) + E(\rho, \rho_a)$. We find that it can be accurately represented by $E(\rho/\rho_a)$. In order to validate these approximations, we display in Fig. 9 both $L(\rho, \rho_a) = (1/\pi)[E(\rho/\rho_a) - E(\rho)\rho_a]$ and $M(\rho,\rho_a) = \sum_{s=1}^{\infty} G_s(J_0(\lambda_s\rho)\sinh^2\gamma_s/\lambda_s\Omega_s)$ for all values of ρ and ρ_a in the intervals $[0; \rho_a]$ and $[0.1; 0.5]$, respectively.

Finally, the expression for the elastic punching in Eq. (35) for $\rho \leq \rho_a$ reduces to

$$p_z = \frac{2}{\pi^2}\frac{1-\nu}{\mu}\frac{1}{R\rho_a}\left[E\left(\frac{\rho}{\rho_a}\right) - E(\rho)\rho_a\right]F. \quad (41)$$

The average displacement under the specimen of radius α is obtained by integrating Eq. (41) over the specimen area: $p(t) = (1/\pi a^2)\int_0^a 2\pi p_z r dr$. This gives:

$$p(t) = K_p F(t), \quad (42)$$

where

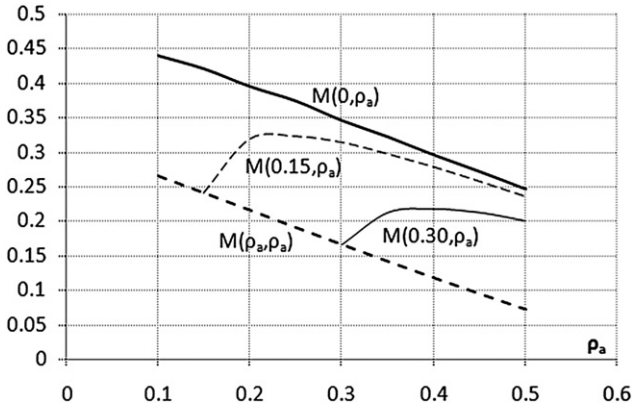

Fig. 7. Values of M(ρ, ρ_a) for $\rho = 0$, 0.15, 0.30, ρ_a.

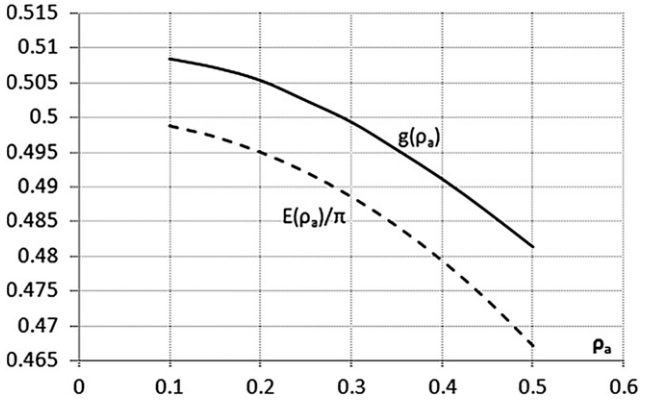

Fig. 8. Values of $g(\rho)$ for $\rho = \rho_a$.

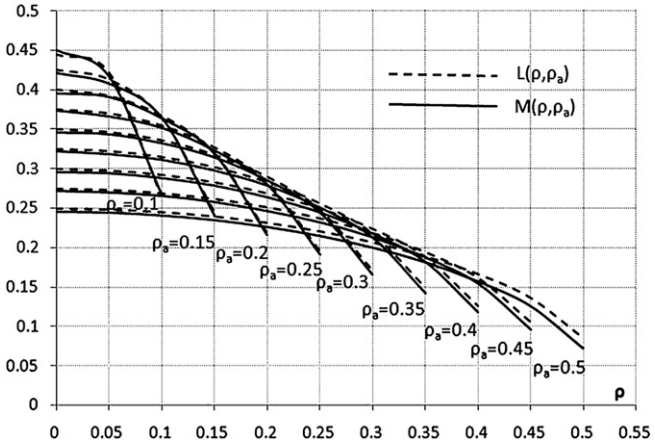

Fig. 9. Exact and approximate generating functions of the displacement p_z.

$$K_p = \frac{4}{3\pi^2}\frac{1-\nu}{a\rho_a\mu}\left[2\rho_a - \left(\rho_a^2+1\right)E(\rho_a) - \left(\rho_a^2-1\right)K(\rho_a)\right]. \quad (43)$$

Here $E(\rho_a)$ is the complete elliptic integral of the second kind: $E(\rho_a) = \int_0^{\pi/2}\sqrt{1-\rho_a^2\sin^2\theta}\,\mathrm{d}\theta$, and $K(\rho_a)$ is the complete elliptic integral of the first kind: $K(\rho_a) = \int_0^{\pi/2}\frac{\mathrm{d}\theta}{\sqrt{1-\rho_a^2\sin^2\theta}}$.

An analysis of the behavior of the short and long term displacement solutions in the vicinity of t_1 is given in Appendix 2.

7. Application to SHPB

Based on Eq. (42): $p(t) = K_pF(t)$, the displacement $u(t)$ obtained by the SHPB standard processing at each face of the sample can be corrected as follows, for $t > t_1$:

$$d_{t>t_1}(t) = u(t) + p(t) = u(t) + K_pF(t). \quad (44)$$

A dynamic numerical simulation is performed with Abaqus explicit code, in order to illustrate this result, for a cylinder of diameter 50 mm subjected to uniform distributions of pressure of diameters 15 and 25 mm, of the same force magnitude (see Appendix 3 for details). Fig. 10 shows the average displacement as calculated with formula (44); for $t < t_1$ the solutions given by Eq. (18) and (20) are used. The 1-D displacement at large distance from the impact zone as it is given by the SHPB processing, $u(t) = (1/\pi R^2\rho c_0)\int_0^t F(\tau)\mathrm{d}\tau$ is also shown.

This simulation confirms that the closed-form solution is almost equal to the one given by the numerical simulation (which is supposed to accurately describe the real solution). The test lasts 85 μs and simulates the behavior of a brittle material. We purposely chose a short loading duration to conveniently visualize the solutions obtained. In the present case, it appears that the amplitude of the correction is of the order of magnitude of the displacement itself up to a force of about 40 kN (250 or 90 MPa for specimens of 15 mm or 25 mm respectively). In the case of a 25 mm diameter specimen loaded by the same total force, the correction for punching becomes rather small. This result also confirms that there was no need to develop a closed-form formula for ratios a/R greater than 0.5. An accurate correction in the interval $0.5 < a/R < 1$ can be obtained through linear interpolation between the correction for $a/R = 0.5$ and the value zero for $a/R = 1$. The distance between the corrected displacement $d(t)$ and the 1-D displacement $u(t)$ given by the SHPB, constitutes the elastic punching $p(t)$ that vanishes when $a = R$.

7.1. Practical implementation of the displacement correction

Now that the elastic punching $p(t)$ is obtained, it has to be incorporated to the end displacement of the bar. In the case of SHPB, both displacements at input and output faces of the specimen are concerned.

An example of the strain recorded at a long distance from the bar end (5 diameters) is given in Fig. 11. We observe that it shows a "foot", at the beginning of the curve. It corresponds to the time (same order of magnitude as t_1) needed to reach a homogeneous state of stress along the radius of the bar. In other words, this result expresses the fact that there is a delay between the beginning of the loading and the one expected from the 1-D analysis, since the wave-guide solution effectively begins after a time of the order of t_1. This is in agreement with some other results or remarks found in the literature [1,27].

When the force is known, the calculated elastic punching (the sum of the elastic punching calculated for each bar) can be used for

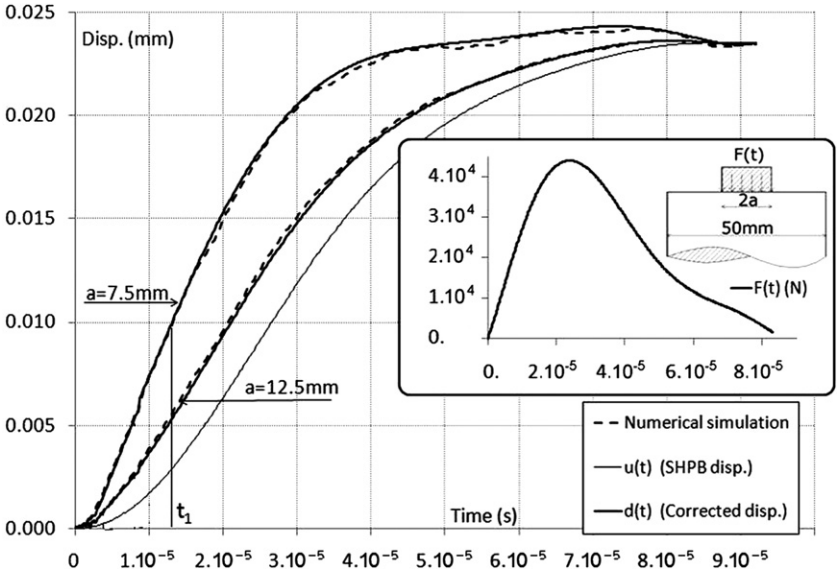

Fig. 10. Numerical, analytical and 1-D average displacements under disks of pressure of diameters 15 and 25 mm, applied on a 50 mm diameter cylinder, according to the same time-dependent function.

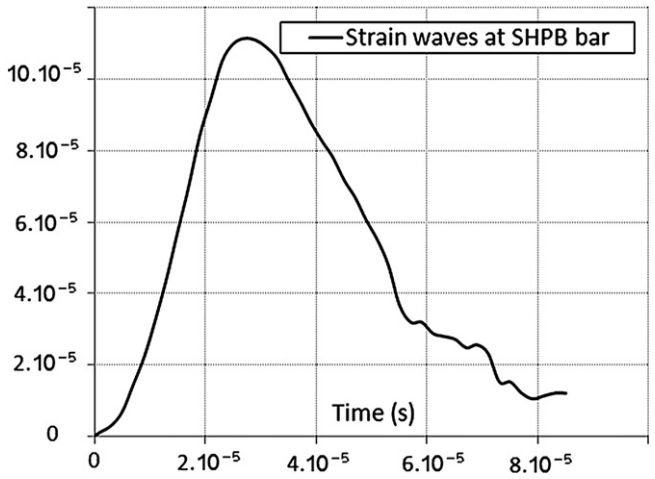

Fig. 11. Strain recorded by axial gages at long distance from the bar end (same loading as for Fig. 9).

the determination of the strain of the specimen, all along the test duration. Note that if the bars have different diameters, the punching will not be the same for both bars.

In Fig. 12, the shape of one bar face is shown. If we consider the case of two identical bars and we denote by l_0 the initial length of the specimen, its current length becomes $l(t) = l_0 + u_o(t) - u_i(t) + 2p(t)$ where $u_i(t)$ and $u_o(t)$ are the displacements of the input and output bars faces, respectively, derived from the standard SHPB analysis. The value $l_0 + u_o(t) - u_i(t)$ therefore under-estimates the length of the specimen. Consequently the real strain in the specimen is less than that given by the classical SHPB analysis, as expected if the bar ends indent.

Recall that $p(t) = K_p F(t)$, where K_p defined in Eq. (43) is a function of the specimen and bar diameters and of the elastic properties of the bar. Clearly, $1/K_p$ represents the stiffness associated with punching.

Thus, for given bars and specimen, the punching effect is equivalent to that of a spring of stiffness $1/K_p$ acting between each bar and the specimen. It explains why SHPB processing without punching corrections leads to underestimated Young's modulus for the specimen. Indeed, for input and output bars with the same impedance, $1/E_{real} = 1/E_{apparent} - 1/E_{punch}$, where $E_{punch} = l_s/2K_p\pi^2 a$,

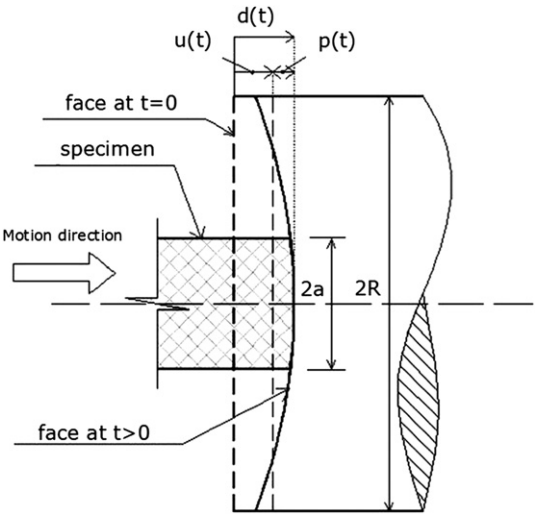

Fig. 12. Schematic view of the output bar end face displacement during a SHPB experiment.

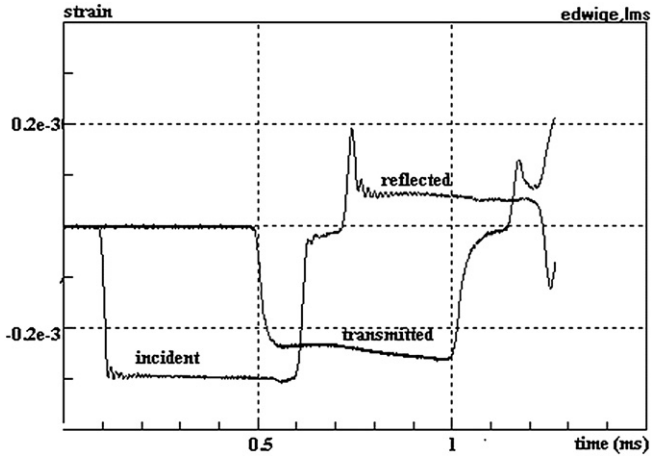

Fig. 13. Basic recorded waves of the test "Steel_08" – see Appendix 4 for technical details.

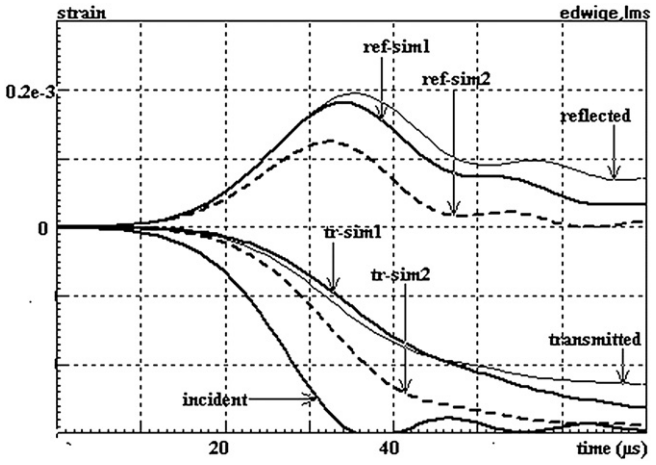

Fig. 14. Waves at bar ends (test "Steel_08").

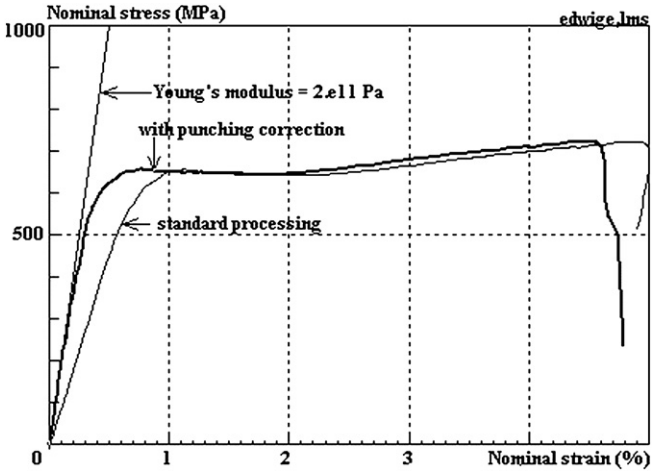

Fig. 15. Nominal stress–strain curve: influence of the punching correction.

l_s, is the specimen length, E_{real} is the real modulus, $E_{apparent}$ that deduced from standard SHPB processing.

Taking account of punching, classical formulas used to derive forces and velocities at bar ends from measured strains become

$$F_i(t) = A_i E_i(\varepsilon_i(t) + \varepsilon_r(t))$$

$$V_i(t) = -c_{0i}(\varepsilon_i(t) - \varepsilon_r(t)) + K_{pi}\frac{\mathrm{d}F_i(t)}{\mathrm{d}t} \quad (45)$$

at the input interface and

$$F_o(t) = A_o E_o \varepsilon_t(t)$$

$$V_o(t) = -c_{0o}\varepsilon_t(t) - K_{po}\frac{\mathrm{d}F_o(t)}{\mathrm{d}t} \quad (46)$$

at the output interface.

Note that in these expressions, F_i and F_o are positive in tension. V_i and V_o are the velocities of the input face of the specimen and of the output face of the specimen, respectively, both positive in the direction from the input bar towards the output bar. The nominal strain rate is then $(V_o - V_i)/l_s$.

7.2. Experimental illustration and applications

In the SHPB processing procedure used in our laboratory, the waves are first transported to bar ends, taking account of dispersion. For an improved shifting of the waves, this procedure involves a transient calculation called "elastic simulation" [9]. The incident wave at the input face of the specimen is used in a 1-D

Summary of main results for SHPB

We consider a classical SHPB apparatus where input and output bars are identical with diameter D and with ρ, ν and E the density, Poisson ratio and Young's modulus, respectively, of their material. The geometrical characteristics of the specimen are d, l_s and S_s, corresponding to its diameter, length and cross sectional area, respectively.

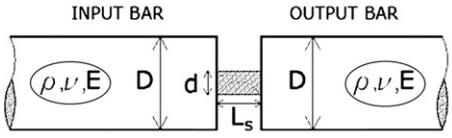

At any time throughout the experiment, the strain of the sample is obtained as

$$\epsilon(t) = \epsilon_{SHPB}(t) - \epsilon_{punch.}(t)$$

where

- $\epsilon_{punch.}(t) - 2K_p\dfrac{\sigma_{SHPB}(t)S_s}{l_s}$
- $\epsilon_{SHPB}(t)$ and $\sigma_{SHPB}(t)$ are the strain and stress, respectively, obtained by standard SHPB formulas.
- $K_p = \dfrac{16}{3\pi^2}\dfrac{1-\nu^2}{dE}H_p(\dfrac{d}{D})$

$$H_p(x) = 2 - (x + \frac{1}{x})E(x) - (x - \frac{1}{x})K(x)$$

$$E(x) = \int_0^{\frac{\pi}{2}} \sqrt{1 - x^2\sin^2\theta}\,d\theta,\ K(x) = \int_0^{\frac{\pi}{2}} \frac{d\theta}{\sqrt{1 - x^2\sin^2\theta}}$$

Tabulated results for the function $H_p(x)$ are given in the table underneath.
Values for $0.5 < x \leq 1$ are obtained by linear interpolation.

x	0.10	0.15	0.20	0.25	0.30	0.35	0.40	0.45	0.50	0.60	0.70	0.80	0.90	1.00
$H_p(x)$	1.765	1.648	1.531	1.416	1.301	1.188	1.076	0.967	0.860	0.688	0.516	0.344	0.172	0

Fig. 16. Summary of main results for SHPB.

transient simulation assuming an elastic behavior of the specimen. This calculation provides reflected and transmitted waves as they would be obtained with an elastic specimen of known Young's modulus.

In the example the details of which are given in Appendix 4, the recorded waves of a test on a steel specimen ($a/R = 0.25$) are shown (Fig. 13).

The results of the elastic simulation are presented (with a Young's modulus of 200 GPa, as expected for a steel specimen) in Fig. 14: "incident", "reflected" and "transmitted" show real waves."tr-sim1" and "ref-sim1" show simulated transmitted and reflected waves taking account of punching. "tr-sim2" and "ref-sim2" show simulated transmitted and reflected waves without punching. It is observed that considering punching provides waves in good agreement with the real ones, at the early instants of the test.

In Fig. 15, it is shown that the punching correction is significant, as it was expected with a specimen diameter smaller than that of the bars. When a test is processed with a specimen that has the same diameter than the bar, there is no punching effect, and one recovers directly the expected modulus.

The main results, for a possible easier implementation in SHPB processing, are summarized in Fig. 16.

8. Conclusion

The problem of the local punching of a bar axially loaded at one end has been investigated. When a known axial stress is dynamically applied on a circular central part of a bar end, it induces an axial displacement which varies with the radius of the loaded area. The effect of punching is the same as that of a hidden spring inside the bar end. A closed-form approximate expression for the displacement due to punching, depending on the mechanical parameters of the bar and of the parameters of the loading is given. It can be easily applied to SHPB testing. It allows for the punching correction and, consequently, for a direct measurement of material properties at low strains, in particular the Young's modulus.

Acknowledgements

The authors are grateful to Professor Bengt Lundberg (Uppsala University, Sweden) for fruitful discussions and his careful reading of the final paper.

Appendix 1. Calculations details for solution of Problem A

The parameters A and B in Eqs. (16) and (19) are obtained with the help of the boundary conditions for $\widetilde{\overline{\sigma}}_z$ and $\widetilde{\overline{\sigma}}_{rz}$ at $z = 0$. Let's write the expressions for the normal and shear stress in terms of the displacements as:

$$\sigma_z = \lambda\left(\frac{\partial u_r}{\partial r} + \frac{u_r}{r}\right) + (\lambda + 2\mu)\frac{\partial u_z}{\partial z} \tag{47}$$

$$\sigma_{rz} = \mu\left(\frac{\partial u_r}{\partial z} + \frac{\partial u_z}{\partial r}\right) \tag{48}$$

By multiplying Eqs. (47) and (48) by $rJ_0(\xi r)$ and $rJ_1(\xi r)$, respectively and then applying the Laplace transform and integrating with respect to r from 0 to ∞, we obtain

$$\widetilde{\overline{\sigma}}_z = \lambda\xi\widetilde{\overline{u}}_r + (\lambda + 2\mu)\frac{\partial\widetilde{\overline{u}}_z}{\partial z} \tag{49}$$

$$\widetilde{\overline{\sigma}}_{rz} = \mu\frac{\partial\widetilde{\overline{u}}_r}{\partial z} - \mu\xi\widetilde{\overline{u}}_z \tag{50}$$

Applying Laplace and Hankel transforms on boundary condition (Eq. (9)), we obtain

$$\overline{\sigma}_z = \frac{\alpha}{s^2}H(a - r) \tag{51}$$

$$\widetilde{\overline{\sigma}}_z = \frac{a\alpha}{\xi s^2}J_1(\xi\alpha). \tag{52}$$

Substituting in Eqs. (49) and (50) the expressions of $\widetilde{\overline{u}}_r$ and $\widetilde{\overline{u}}_z$ found in Eqs. (16) and (17), then applying the boundary conditions we obtain:

$$2kqA + \left(\frac{s^2}{c_2^2} + 2\xi^2\right)B = 0 \tag{53}$$

$$\left(\frac{s^2}{c_2^2} + 2\xi^2\right)A + 2\xi^2 B = -\frac{a\alpha}{\mu s^2}J_1(\xi a). \tag{54}$$

Solving Eqs. (53) and (54) we obtain

$$A = -\frac{a\alpha}{\mu s^2}J_1(\xi a)\frac{\frac{s^2}{c_2^2} + 2\xi^2}{\left(\frac{s^2}{c_2^2} + 2\xi^2\right)^2 - 4kq\xi^2} \tag{55}$$

$$B = \frac{a\alpha}{\mu s^2}J_1(\xi a)\frac{2kq}{\left(\frac{s^2}{c_2^2} + 2\xi^2\right)^2 - 4kq\xi^2} \tag{56}$$

Substituting these expressions for A and B into Eqs. (16) and (17), we get:

$$\widetilde{\overline{u}}_r = \frac{-\frac{a\alpha}{\mu s^2}J_1(\xi a)}{\left(\frac{s^2}{c_2^2} + 2\xi^2\right)^2 - 4kq\xi^2}\left\{\left(\frac{s^2}{c_2^2} + 2\xi^2\right)e^{-kz} - 2kqe^{-qz}\right\} \tag{57}$$

$$\widetilde{\overline{u}}_z = \frac{k}{\xi}\frac{-\frac{a\alpha}{\mu s^2}J_1(\xi a)}{\left(\frac{s^2}{c_2^2} + 2\xi^2\right)^2 - 4kq\xi^2}\left\{\left(\frac{s^2}{c_2^2} + 2\xi^2\right)e^{-kz} - 2\xi^2 e^{-qz}\right\}. \tag{58}$$

By applying the inverse Laplace transform to Eq. (58), we obtain:

$$\widetilde{\overline{u}}_z = \frac{a\alpha}{2\pi i\mu}\frac{J_1(\xi a)}{\xi}\int_{\gamma - i\infty}^{\gamma + i\infty}\frac{k}{s^2}\frac{\left(\frac{s^2}{c_2^2} + 2\xi^2\right)e^{-kz} - 2\xi^2 e^{-qz}}{\left(\frac{s^2}{c_2^2} + 2\xi^2\right)^2 - 4kq\xi^2}e^{st}ds. \tag{59}$$

This complex integral is similar to the one obtained by Eason [18] in the case of a half-plane loaded by a sudden constant force. In the current problem, we have a double pole at $s = 0$ and simple poles at $s = \pm i\xi c_R$, where c_R is the speed of Rayleigh waves. We have branch points at $s = \pm i\xi c_2$ and $s = \pm i\xi c_1$ resulting from variables $_k$ and $_q$ in the numerator. These two variables are square-roots functions of the complex number s and therefore are multi-valued at the point $s = 0$.

Consider the integral

$$I=\int_{\gamma-i\infty}^{\gamma+i\infty}\frac{k}{s^2}\frac{\left(\frac{s^2}{c_2^2}+2\xi^2\right)e^{-kz}-2\xi^2e^{-qz}}{\left(\frac{s^2}{c_2^2}+2\xi^2\right)^2-4kq\xi^2}e^{st}\mathrm{d}s=\int_{\gamma-i\infty}^{\gamma+i\infty}g(s)\mathrm{d}s \quad (60)$$

along the vertical path of the contour S (Fig. 17). Applying Cauchy's residue theorem, we obtain

$$\oint_s g(s)\mathrm{d}s \;=\; 2\pi i[Res[g,0]+Res[g,\pm i\xi c_R]] \quad (61)$$

$$Res[g,0] \;=\; \lim_{s\to 0}\frac{\partial}{\partial s}\left[s^2g(s)\right] \;=\; \frac{c_1^2+\xi z(c_1^2-c_2^2)}{2\xi(c_1^2-c_2^2)}e^{-\xi z}t. \quad (62)$$

$$\begin{aligned}Res[g,\pm i\xi c_R] \;&=\; \lim_{s\to\pm i\xi c_R}\frac{\mathrm{num}[g(s)]}{\frac{\partial}{\partial s}(\mathrm{denom}[g(s)])}\\ &=\; -\frac{\pi k_1\left[\left(2-\frac{c_R^2}{c_2^2}\right)e^{-k_1\xi z}-2e^{-q_1\xi z}\right]}{4\xi^2c_R^3\left[\frac{1}{c_2^2}\;\;2-\frac{c_R^2}{c_2^2}\right)-\frac{q_1}{k_1c_1^2}-\frac{k_1}{q_1c_2^2}\right]}\sin(\xi c_Rt),\end{aligned} \quad (63)$$

where $k_1 \;=\; \sqrt{1-(c_R^2)/(c_1^2)}$; $q_1 \;=\; \sqrt{1-(c_R^2)/(c_2^2)}$.

Integrals along the horizontal path vanish since $\gamma\to 0$; it is the same for the integrals along the contour at infinity and around the branches. In the present problem, we are interested in calculating the axial component of the displacement at the surface $z=0$; hence we are mainly concerned with the residue of $g(s)$ at the Rayleigh pole, which describes the contribution of the surface waves to the total displacement, and also at large times which corresponds to $s=0$. The displacements given by the remaining integrals are related to dilatational and shear waves; they are neglected since their contribution to the surface displacement is negligible, as it has been shown [17,18]. The residue of $g(s)$ at $s=0$ and can be designed as the pseudo-static value of the displacement; this point is clarified here after. The integral Eq. (60) becomes

$$I\approx\oint_s g(s)\mathrm{d}s \;=\; 2\pi i[Res[g,0]+Res[g,\pm i\xi c_R]]. \quad (64)$$

Substituting Eq. (64) in Eq. (59) we obtain

$$\widetilde{u}_z\approx -\frac{a\alpha}{\mu}\frac{J_1(\xi a)}{\xi}[Res[g,0]+Res[g,\pm i\xi c_R]] \quad (65)$$

With Eqs. (62) and (63) inserted, Eq. (65) gives

$$\begin{aligned}\widetilde{u}_z\approx -\frac{a\alpha}{\mu}\frac{J_1(\xi a)}{\xi}\Bigg[&\frac{c_1^2+\xi z(c_1^2-c_2^2)}{2\xi(c_1^2-c_2^2)}e^{-\xi z}t\\ &-\frac{\pi k_1\left[\left(2-\frac{c_R^2}{c_2^2}\right)e^{-k_1\xi z}-2e^{-q_1\xi z}\right]\sin(\xi c_Rt)}{4\xi^2c_R\left[\frac{c_R^2}{c_2^2}\left(2-\frac{c_R^2}{c_2^2}\right)-\frac{q_1c_R^2}{k_1c_1^2}-\frac{k_1c_R^2}{q_1c_2^2}\right]}\Bigg]\end{aligned} \quad (66)$$

Applying the inverse Hankel transform leads to

$$\begin{aligned}\widetilde{u}_z\approx -\frac{a\alpha}{\mu}\int_0^\infty J_0(\xi r)J_1(\xi a)\Bigg[&\frac{c_1^2+\xi z(c_1^2-c_2^2)}{2\xi(c_1^2-c_2^2)}e^{-\xi z}t\\ &-\frac{\pi k_1\left[\left(2-\frac{c_R^2}{c_2^2}\right)e^{-k_1\xi z}-2e^{-q_1\xi z}\right]\sin(\xi c_Rt)}{4\xi^2c_R\left[\frac{c_R^2}{c_2^2}\left(2-\frac{c_R^2}{c_2^2}\right)-\frac{q_1c_R^2}{k_1c_1^2}-\frac{k_1c_R^2}{q_1c_2^2}\right]}\Bigg]\mathrm{d}\xi\end{aligned} \quad (67)$$

The two integrals of Eq. (67) will be evaluated at $z=0$.

Integrals of the type $\int_0^\infty(1/\xi^k)J_i(\xi r)J_j(\xi a)\mathrm{d}\xi$ are discontinuous; their solutions are given by Watson [28], §13.4. For $r\le a$; we have $\int_0^\infty(1/\xi)J_0(\xi r)J_1(\xi a)\mathrm{d}\xi \;=\; (2/\pi)E(r/a)$, where $E(r/a)$ is the complete elliptic integral of the second kind: $E(\rho_a) \;=\; \int_0^{\pi/2}\sqrt{1-\rho_a^2\sin^2\theta}\mathrm{d}\theta$. The first term of integral (Eq. (67)) becomes

$$\int_0^\infty\frac{1}{\xi}J_0(\xi r)J_1(\xi a)\frac{c_1^2}{2(c_1^2-c_2^2)}t\mathrm{d}\xi \;=\; \frac{2(1-\nu)}{\pi}E\left(\frac{r}{a}\right)t. \quad (68)$$

The integral $\int_0^\infty(1/\xi^2)J_0(\xi r)J_1(\xi a)\sin(\xi c_Rt)\mathrm{d}\xi$ appears in the second term of Eq. (67). Using the property [28], §10: $J_0(\xi r)J_1(\xi a) \;=\; (1/\pi)\int_0^\pi J_1(\xi W)(a-r\cos\phi/W)\mathrm{d}\phi$,

where $W \;=\; \sqrt{r^2+a^2-2ar\cos\phi}$, we can write:

$$\begin{aligned}&\int_0^\infty\frac{1}{\xi^2}J_0(\xi r)J_1(\xi a)\sin(\xi c_Rt)\mathrm{d}\xi\\ &\quad=\;\frac{1}{\pi}\int_0^\pi\frac{a-r\cos\phi}{W}\mathrm{d}\phi\int_0^\infty\frac{J_1(\xi W)}{\xi^2}\sin(\xi c_Rt)\mathrm{d}\xi\end{aligned} \quad (69)$$

For $c_Rt<(a+r)$,

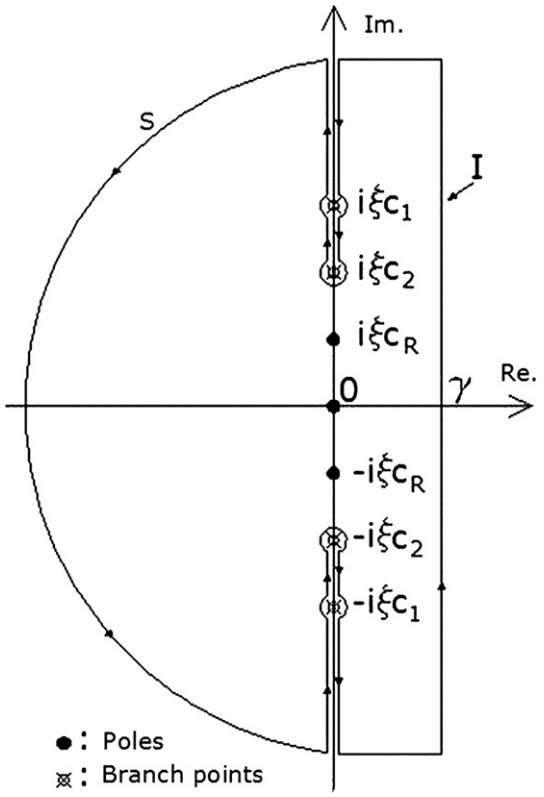

Fig. 17. Mapping on s-plane.

$$\int_0^\infty \frac{J_1(\xi W)}{\xi^2}\sin(\xi c_R t)\mathrm{d}\xi = \frac{1}{2W}\left(c_R t\sqrt{W^2 - c_R^2 t^2} + W^2 \arcsin\frac{c_R t}{W}\right)$$

For $c_R t \geq (a + r)$,

$$\int_0^\infty \frac{J_1(\xi W)}{\xi^2}\sin(\xi c_R t)\mathrm{d}\xi = \frac{\pi}{4}W$$

Introducing these results in Eq. (69), we get:

$$\int_0^\infty \frac{1}{\xi^2}J_0(\xi r)J_1(\xi a)\sin(\xi c_R t)\mathrm{d}\xi = \begin{cases} \dfrac{1}{2\pi}\displaystyle\int_0^\pi \frac{a - r\cos\phi}{W^2}\left(c_R t\sqrt{W^2 - c_R^2 t^2} + W^2\arcsin\frac{c_R t}{W}\right)\mathrm{d}\phi, \\ \quad c_R t < (a + r) \\ \dfrac{\pi}{4}a, \quad c_R t \geq (a + r) \end{cases} \tag{70}$$

Finally, introducing Eqs. (68) and (70) in (67) we obtain the axial surface displacement under a specimen of radius a, at radius r and at time t:

$$u_z = -\frac{a\alpha}{\mu}\left\{\frac{2}{\pi}(1-\nu)E\left(\frac{r}{a}\right)t + \frac{k_1 c_R \displaystyle\int_0^\pi \frac{a - r\cos\phi}{W^2}\left(c_R t\sqrt{W^2 - c_R^2 t^2} + W^2\arcsin\frac{c_R t}{W}\right)\mathrm{d}\phi}{8c_2^2\left[\frac{c_R^2}{c_2^2}\left(2 - \frac{c_R^2}{c_2^2}\right) - \frac{q_1 c_R^2}{k_1 c_1^2} - \frac{k_1 c_R^2}{q_1 c_2^2}\right]}\right\} \tag{71}$$

for $c_R t < (a + r)$

$$u_z = -\frac{a\alpha}{\mu}\left\{\frac{2}{\pi}(1-\nu)E\left(\frac{r}{a}\right)t + \frac{\pi^2 k_1 c_R a}{16c_2^2\left[\frac{c_R^2}{c_2^2}\left(2 - \frac{c_R^2}{c_2^2}\right) - \frac{q_1 c_R^2}{k_1 c_1^2} - \frac{k_1 c_R^2}{q_1 c_2^2}\right]}\right\} \tag{72}$$

for $c_R t \geq (a + r)$

Appendix 2. Analysis of the corrected displacement function d(t) at the neighborhood of t_1

In the solution of problem A of this paper, the instant of transition between the transient state and the pseudo quasi-static situation at the end of the cylinder, has been estimated as $t_1 = (2(R - a))/(c_R)$. It cannot be expected that the displacements given by Eqs. (22) and (44) have exactly the same value at $t = t_1$.

We calculate the function $\epsilon_{t_1} = (d_{t>t_1}(t_1) - d_{t\leq t_1}(t_1))/(d_{t\geq t_1}(t_1))$ (Fig. 18) that expresses the relative distance at $t = t_1$, between the short and long time displacement solutions. We use for the speed of Rayleigh waves the accurate approximation [29] $c_R = (0.87 + 1.12\nu/1 + \nu)c_2$, and we keep in mind that in the neighborhood of t_1 we still can approximate the real applied force $F(t)$ by a linear loading function of time: $F(t) = \pi a^2 \alpha t$ Then, $u(t)$ can be written: $u(t) = (1/\pi R^2 \rho c_0)\int_0^t F(\tau)\mathrm{d}\tau = (c_0\rho_a^2\alpha/4(1+\nu)\mu)t^2$.

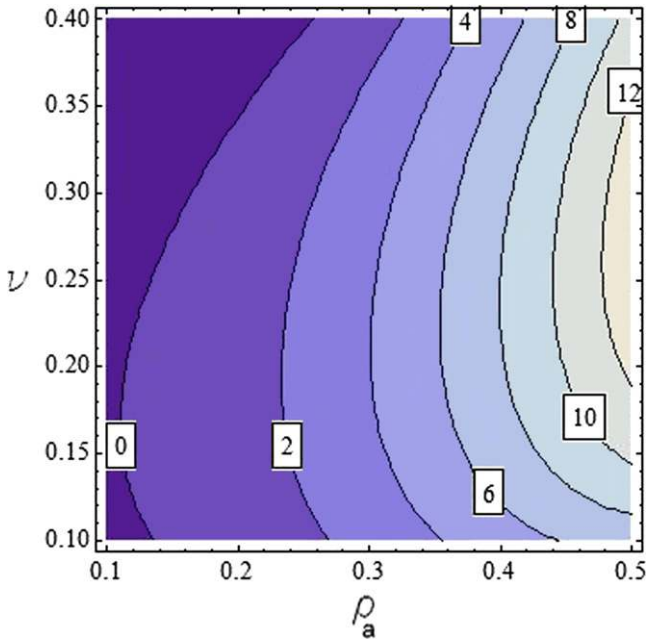

Fig. 18. Percentage of the relative error ($100\epsilon_{t_1}$) on the displacement at $t = t_1$ between the solutions at short and long times.

Fig. 18 shows that depending on ρ_a and ν, the displacements given by solutions (20) and (44) at $t = t_1$ are not equal. For a steel bar ($\nu = 0.3$) the relative distance between both solutions varies between 0 and 12%, according to the diameter of the sample (relatively to that of the bar).

This gap is observed at the very early instants of the test and does not last more than a few microseconds. Furthermore, at this time, the value of the strain is still very small (typically less than 0.1% for standard specimen). This point can be checked with the results of the numerical simulation (Ref. part 7 of the present paper).

Appendix 3. Information about the numerical simulations carried out

Numerical calculations are performed using the general-purpose finite element code Abacus/Explicit version 6.7, with element type CAX4R (axis symmetric element, reduced integration). An automatic time-integration scheme offered by the software is used throughout the simulations. A structured meshing technique was used with square meshes of 0.5 mm side. Non-linear

Table 1
"Steel_08".

Element	Length (m)	Diameter (m)	Mass density (kg/m^3)	Wave speed (m/s)	Gage position (m)
Striker	1.204	0.0203	7960	4795	
Input bar	3.01	0.02017	7960	4795	1.495
Output bar	2.009	0.02017	79607	4795	0.375
Specimen	0.00645	0.00513	7805		

Striker speed: 2.79 m/s.

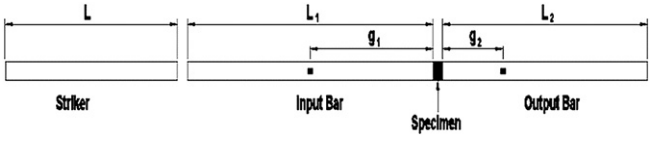

Fig. 19. Basic schematics of the experimental equipment.

geometry effects were not considered stiffness matrix remaining the same during the calculations – since in the analytical solutions we consider the initial and final deformed shape of the cylinder as identical (small deformations hypothesis). The mesh distortion correction is automatically controlled by the software and was checked to be without influence on the results.

The loading was introduced by the mean of tabulation, and did not lead to numerical perturbations that are usually induced by the high frequencies, since the beginning of the load is mainly a linear function of time. Displacements are considered at the nodes located at the loaded surface of the cylinder, and not at the integration points.

Appendix 4. Information about the experiments carried out

The characteristics of the steel specimen are given in the Table 1 below. The SHPB setup is made of steel bars. In Fig. 19 the basic schematics of the experimental equipment is shown:

- L_i–the length of the bars and striker
- g_i–the distance between specimen faces and the strain gages

References

[1] Skalak R. Longitudinal impact of a semi-infinite circular elastic bar. Journal of Applied Mechanics 1957;24:59–64.
[2] Folk R, Fox G, Shook CA, Curtis CW. Elastic strain produced by sudden application of pressure to one end of a cylindrical bar. I. Theory. Journal of the Acoustical Society of America 1958;30:552–8.
[3] Jones OE, Norwood FR. Axially symmetric cross-sectional strain and stress distributions in suddenly loaded cylindrical elastic bars. Journal of Applied Mechanics 1967;34:718–24.
[4] Kennedy LW, Jones OE. Longitudinal wave propagation in a circular bar loaded suddenly by a radially distributed end stress. Journal of Applied Mechanics 1969;36:470–8.
[5] Gama B, Lopatnikov S, Gillespie JW. Hopkinson bar experimental technique: a critical review. Applied Mechanics Reviews 2004;57:223–50.
[6] Flynn PD, Frocht MM. On Saint Venant's Principle under dynamic conditions. Experimental Mechanics 1961;1:16–20.
[7] Field JE, Proud WG, Walley SM, Goldrein HT. Review of experimental techniques for high rate deformation and shock studies. In: Nowacki WK, Klepaczko JR, editors. New experimental methods in material dynamics and impact. Warsaw, Poland: Institute of Fundamental Technological Research; 2001. p. 109–177,.
[8] Rota L. Application de méthodes inverses au dépouillement de l'essai aux barres de Hopkinson. PhD thesis, Ecole Polytechnique; 1997.
[9] Zhao H, Gary G. On the use of SHPB technique to determine the dynamic behavior of the materials in the range of small strains. International Journal of Solids & Structures 1996;33:3363–75.
[10] Gary G. David, instruction manual. Palaiseau, France; 2005. LMS, FX Conseil ed., 7 r. St.Dominique, 75007 Paris.http://www.lms.polytechnique.fr/equipe/dynamique/david.html.
[11] Buchar J, Bílek Z, Dusek F. Mechanical behavior of metals at extremely high strain rates (Section 3.2). Switzerland: Trans Tech Publications; 1986.
[12] Oliver J. Elastic wave dispersion in a cylindrical rod by a wide-band short-duration pulse technique. Journal of the Acoustical Society of America 1957;29:189–94.
[13] Safford NA. Materials testing up to 10^5 s^{-1} using a miniaturised Hopkinson bar with dispersion corrections. In: Zhang G, Huang S, editors. Proceedings of the second international symposium on intense dynamic loading and its effects. Chengdu, P.R. China: Sichuan University Press; 1992. p. 378–83.
[14] Field JE, Palmer SJP, Pope PH, Sundararajan R, Swallowe GM. Mechanical properties of PBXs and their behaviour during drop-weight impact. In: Short JM, editor. Proceedings of the eighth symposium (international) on detonation. White Oak, Maryland, USA: Naval Surface Weapons Center; 1985. p. 635–644,.
[15] Knowles JK, Horgan CO. On the exponential decay of stresses in circular elastic cylinders subject to axisymmetric self-equilibrated end loads. International Journal of Solids and Structures 1969;5:33–50.
[16] Kolsky H. An investigation of mechanical properties of materials at very high rates of loading. Proceedings of the Philosophical Society of London B 1949:62676–700.
[17] Mitra M. Disturbance produced in an elastic half-space by impulsive normal pressure. Proceedings of the Cambridge Philosophical Society 1964;60:683–96.
[18] Eason G. The displacements produced in an elastic half-space by a suddenly applied surface force. Journal of the Institute of Mathematics and Its Applications 1966;2:299–326.
[19] Timoshenko SP, Goodier JN. Theory of elasticity. 3rd ed. New York: McGraw-Hill; 1970.
[20] Lurie AI. Theory of elasticity. 2nd ed. Springer; 1999.
[21] Little RW, Childs SB. Elastostatic boundary region problem in solid cylinders. Quarterly of Applied Mathematics 1967;25:261–74.
[22] Horvay G, Mirabal JA. The end problem of cylinders. Journal of Applied Mechanics 1958;25:561–71.
[23] Roark A, Warren WE. A note on the end effect in isotropic cylinders. AIAA Journal 1967;5:1484–6.
[24] Benthem JP, Minderhood P. The problem of the solid cylinder compressed between rough rigid stamps. International Journal of Solids and Structures 1972;8:1027–42.
[25] Wei XX, Chau KT, Wong RHC. Analytic solution for axial point loads strength test on solid circular cylinders. Journal of Engineering Mechanics 1999;125(12):1349–57.
[26] Love AEH. A treatise on the mathematical theory of elasticity. 4th ed. New York: Dover; 1944.
[27] Bancroft D. The velocity of longitudinal waves in cylindrical bars. Physical Review 1941;59:588–93.
[28] Watson GN. Theory of Bessel functions. Cambridge University Press; 1958.
[29] Graff KF. Wave motion in elastic solids. New York: Dover Publications; 1991.